STARS

University of Central Florida
STARS

Faculty Bibliography 2010s

Faculty Bibliography

1-1-2013

Enhanced Design of Narrowband Filters Based on The Extraordinary Transmission Through Single Fishnet Structures

Nicholas S. Nye
University of Central Florida

Alexandros I. Dimitriadis

Nikolaos V. Kantartzis

Theodoros D. Tsiboukis

Find similar works at: https://stars.library.ucf.edu/facultybib2010

University of Central Florida Libraries http://library.ucf.edu

Recommended Citation

University of Central Florida

STARS
Showcase of Text, Archives, Research & Scholarship

ENHANCED DESIGN OF NARROWBAND FILTERS BASED ON THE EXTRAORDINARY TRANSMISSION THROUGH SINGLE FISHNET STRUCTURES

Nicholas S. Nye[1], Alexandros I. Dimitriadis[2, *], Nikolaos V. Kantartzis[2], and Theodoros D. Tsiboukis[2]

[1]The College of Optics and Photonics (CREOL), University of Central Florida, Orlando, FL 32816, USA

[2]Department of Electrical and Computer Engineering, Aristotle University of Thessaloniki, GR-54124 Thessaloniki, Greece

Abstract—A systematic method for the efficient design of narrowband filters founded on the extraordinary transmission via single fishnet structures (SFSs) is presented in this paper. Essentially, due to its strong resonant behavior, this phenomenon is proven suitable for the implementation of high-Q devices. The new design formulas are derived through the combination of full-wave numerical simulations and curve fitting algorithms. Also, adequate mathematical criteria are defined for the evaluation of the filters' linear performance, indicating that the transmitted electromagnetic waves remain practically undistorted in the frequency band of interest. Then, by exploiting the previously developed relations, proper correction factors are introduced in the existing SFS equivalent circuit expressions, which hardly increase the overall computational complexity. This quantitative modification leads to an enhanced characterization of SFSs, as key components for diverse applications. Finally, several limitations as well as possible ways of extending the featured algorithm to more complicated structures and higher frequency bands are briefly discussed.

1. INTRODUCTION

Fishnet structures are devised from single or stacked metallic plates perforated by periodic sub-wavelength hole arrays. Initially, they have been employed for the realization of low-loss, negative-refractive-index

materials in the microwave, near-infrared, and optical region [1–5]. Nonetheless, such structures should not be confused with the traditional frequency selective surfaces (FSSs), exhaustively studied since the 1950's [6, 7]. Basically, their primary difference stems from the size of the holes, which substantially affects their transmission spectra [8]. Thus, while in traditional FSSs (hole dimensions comparable to the wavelength) the transmission is broadband and the center frequency is low compared to that of the first Wood-Rayleigh anomaly, in fishnet structures (comprising sub-wavelength holes) the transmission bandwidth is very narrow and the center frequency approaches that of the first Wood-Rayleigh anomaly. This unique and beneficial property opens up the possibility of constructing high-quality filters by properly designed fishnet arrangements.

It has been long believed that, according to Bethe's theory [9], the transmission through a sub-wavelength hole array should be insignificant. Hence, the sharp transmission peak originally observed at optical frequencies by Ebbesen et al. [10], given the name extraordinary transmission (ET), came as a real surprise. During the next decade, a lot of noteworthy efforts have been conducted to reveal the underlying physics of this intriguing phenomenon [11, 12]. The most prevalent interpretation has been derived from the generation of surface plasmons on metallic surfaces [13–16] due to the plasma-like behavior of metals at optical frequencies. Yet, experiments showed that the ET phenomenon occurs also at microwave frequencies [17], where metals act as perfect conductors and, therefore, cannot support surface plasmons.

In the light of this perspective, diverse effective diffraction models have been developed to enable thorough electromagnetic computations for a 2-D array of holes [18–22]. These models highlight the importance of periodicity, rather than the excitation of surface plasmons, for the onset of the ET phenomenon. Nevertheless, the concept of surface plasmons has been later extended to the microwave regime in the context of spoof plasmons [23, 24], i.e., surface waves with a plasma-like behavior propagating on the surface of periodically corrugated metals at the perfect conductor limit.

Apart from this ongoing research, serious attention has been recently drawn to the extraction of equivalent circuits that model transmission through fishnet configurations via robust impedance matching schemes [25–28]. Being relatively simple, such models facilitate the analysis and design process of diverse practical components. Besides, in accordance with these equivalent circuits, the periodicity of the resulting device is not a necessary prerequisite for the phenomenon to appear, as also experimentally proven in [29].

Taking into account the prior aspects, it is the aim of this paper to

efficiently exploit the ET through single fishnet structures (SFSs) for the development of high-Q filters via a novel inverse-engineering design method. Therefore, full-wave numerical simulations are conducted and explicit design formulas for the appropriate geometrical dimensions of the SFS are successfully retrieved in terms of curve fitting techniques to fulfill prescribed center frequency and bandwidth criteria. These formulas are valid for the whole microwave spectrum (1–100 GHz), where metals can be treated as perfect conductors, and for very high quality factors (typically $Q > 100$). Moreover, particular attention is devoted to prove the linear performance of the filters in order to assure their suitability for real-world scenarios. Besides, by incorporating the extracted design relations and matching the simulation results with their theoretical counterparts, appropriate correction factors for the established circuit model of the SFS are introduced. This systematic formulation leads to a more accurate and computationally efficient modeling of the critical SFS transmission properties. Finally, possible extensions to more complicated setups, are briefly discussed.

2. CIRCUIT MODEL FOR THE TRANSMISSION THROUGH AN INFINITE SFS

In this section, the circuit model for a thin SFS with square holes, introduced in [26], is briefly discussed. So, let us consider the infinite SFS of Figure 1(a), with unit-cell and hole dimensions a and b,
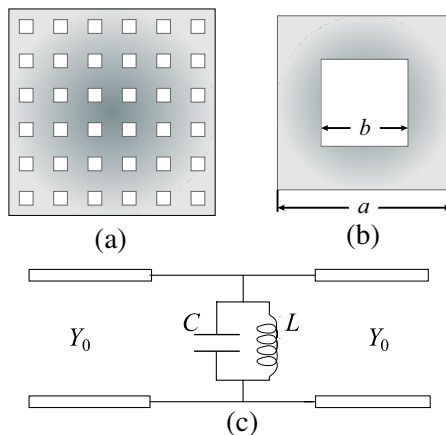

Figure 1. (a) Infinite SFS with square holes (colored area represents metal), (b) its unit-cell with the corresponding dimensions, and (c) the equivalent circuit model derived in [26].

respectively, as shown in Figure 1(b). Since ET is a resonant phenomenon, the transmission through the SFS can be computed with the help of the equivalent LC circuit of Figure 1(c). From a physical point of view, the capacitive term, C, is related to the electrical energy of the bellow-cutoff TM modes excited at the discontinuity plane, while the inductive element, L, is associated with the magnetic energy of the below-cutoff TE modes, respectively. Then, the transmission coefficient, $T(f)$, through the SFS is

$$T(f) = (b_C + b_L + 1)^{-1},$$ (1)

with b_C, b_L the normalized admittances, computed via

$$b_C(x_1, x_2, x_3)$$
$$= \sum_{m=1}^{M} 2y_{0,m}^{\mathrm{TM}}\mathrm{sinc}\left(\frac{m}{x_1}\right) + \sum_{n,m=1}^{N,M} 4y_{n,m}^{\mathrm{TM}}\,\mathrm{sinc}\left(\frac{n}{x_1}\right)\mathrm{sinc}\left(\frac{m}{x_1}\right)\frac{m^2}{n^2+m^2},$$ (2)

$$b_L(x_1, x_2, x_3)$$
$$= \sum_{n=1}^{N} 2y_{n,0}^{\mathrm{TE}}\mathrm{sinc}\left(\frac{n}{x_1}\right) + \sum_{n,m=1}^{N,M} 4y_{n,m}^{\mathrm{TE}}\mathrm{sinc}\left(\frac{n}{x_1}\right)\mathrm{sinc}\left(\frac{m}{x_1}\right)\frac{m^2}{n^2+m^2},$$ (3)

where $x_1 = a/b$, $x_2 = a/\lambda_0$, $x_3 = \lambda_0/\lambda$, $\mathrm{sinc}(x) = \sin(\pi x)/(\pi x)$, and the zero subscript refers to the frequency of ET. Furthermore, N, $M = \lfloor x_1 \rfloor$, with $\lfloor \cdot \rfloor$ representing the integer part of a real number, and y^{TM}, y^{TE} denote the normalized TM, TE modal admittances, correspondingly. In particular, the latter are obtained through

$$y_{n,m}^{\mathrm{TM}}(x_2, x_3) = -j\left[\sqrt{\frac{n+m}{(x_2 x_3)^2} - 1}\right]^{-1},$$ (4)

$$y_{n,m}^{\mathrm{TE}}(x_2, x_3) = j\sqrt{\frac{n+m}{(x_2 x_3)^2} - 1}.$$ (5)

Note that the dependence of b_C and b_L on x_2 and x_3, although not explicitly shown in (2) and (3), occurs due to the analogous form of (4) and (5). Before proceeding with our design algorithm, it is worth discussing the main assumptions under which the equivalent circuit of [26] has been developed, as they will be proven useful for the development and interpretation of the featured procedure.

Firstly, the thickness of the metallic screen is assumed to be very small compared to the unit cell dimensions, in order to obtain the desired narrowband performance of the corresponding devices. Increasing the thickness of the screen allows the propagation of

evanescent waveguide modes through the holes, leading to a more complicated behaviour of the structure. In order to account for these propagation phenomena, the equivalent circuit of Figure 1(c) has to be properly modified [27]. In that case, two closely-spaced peaks appear near the Wood-Rayleigh anomaly, yielding a broadband or even a dual-band performance, which is out of the scope of the present work [30].

Moreover, infinite conductivity for the metallic screen has been implied. When metallic losses are present, they must be included into the model of Figure 1(c) through a resistive element in series with the inductance. Circuit models that capture the appearance of surface plasmons can also be obtained [31, 32]. However, since such an approach is not straightforward, we limit our study to frequencies up to 100 GHz, whereupon metals act as perfect electric conductors.

On the other hand, a normally incident plane wave with its electric field polarized along the x- or y-axis is presumed for the excitation of the SFS. Together with the periodic boundary conditions (PBCs) applied to the unit cell, this excitation is equivalent to the propagation of a TEM mode in a parallel-plate waveguide with a square diaphragm. Due to the symmetry of the structure, only even higher-order TM and TE modes are excited from the diaphragm, with cutoff frequencies

$$f_{m,n} = c\sqrt{\left(\frac{m}{a}\right)^2 + \left(\frac{n}{a}\right)^2}. \tag{6}$$

For frequencies up to the first Wood-Rayleigh anomaly ($f_{\mathrm{WR}} = c/a$), all the corresponding modes are below cutoff. Such evanescent modes exhibit a reactive behavior and store electric and magnetic energy, respectively. The ET phenomenon appears when the electric energy stored in the TM modes becomes equal to the magnetic energy stored in the TE ones; hence, it is a resonant phenomenon.

Finally, the size of the holes, b, is assumed to be small compared to the resonance wavelength ($b \ll \lambda_0$) and, consequently, to the unit cell dimension, a, for the frequencies of interest (small-hole approximation). However, this is not a strict limitation and it can be relaxed up to $b < a/2$, without significantly affecting the accuracy of (1). In fact, this is the reason why only the first $\lfloor x_1 \rfloor$ modes from (4) and (5) need to be taken into account in the modal analysis, as proven in [26].

3. FORMULATION OF THE PROPOSED ALGORITHM

As already stated in Section 1, the purpose of this paper is two-fold; to derive explicit formulas for the geometric parameters of an SFS which satisfy certain design criteria and to provide suitable correction factors for the expressions of the transmission coefficient of the previous

section. These two distinct goals are achieved by the algorithmic steps described in the flowcharts of Figures 2(a) and 2(b), correspondingly.

Specifically, Figure 2(a) illustrates the design procedure presented in Section 4. Initially, simulations with various unit cell and hole dimensions are conducted in order to acquire a relevant number of transmission data sets. Next, the center frequency, f_0, and half-power bandwidth, BW, (hereafter designated as "design parameters" or "design criteria") are extracted from the respective transmission
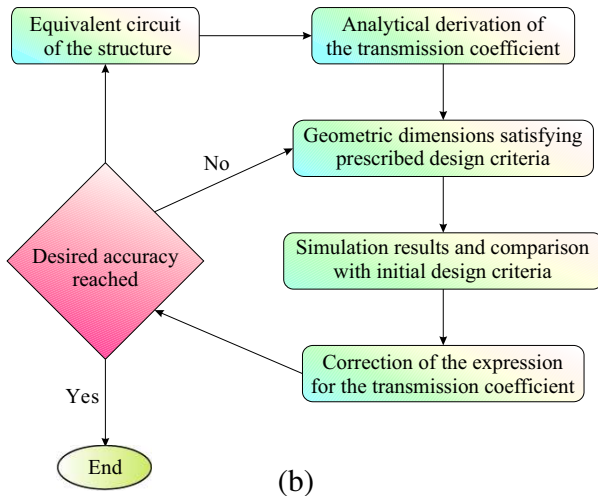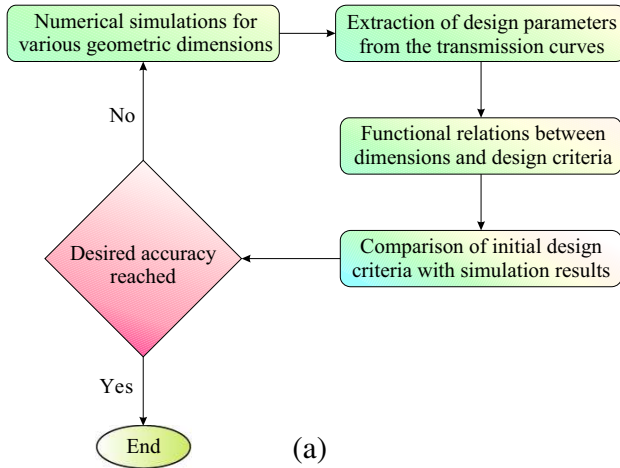

Figure 2. Flowcharts describing (a) the design method of Section 4 and (b) the circuit-model enhancement procedure of Section 5.

curves. From the analysis of the simulation results, functional relations between the design criteria and geometric parameters of the structure are obtained via the appropriate curve fitting algorithms. These relations are, in fact, the desired formulas for the design of narrowband, SFS-based filters. Finally, the output dimensions are utilized in numerical simulations and the properties of the resulting transmission curves are compared with the initial design criteria to verify the accuracy of the algorithm. If its relative error is not satisfactory, further iterations of the process in Figure 2(a) can be performed, by taking into account a larger number of initial transmission data sets, so as to ensure a better convergence of the curve fitting approaches.

On the other hand, Figure 2(b) presents the main stages for the enhancement of the equivalent circuit approach [26], as developed in Section 5. Herein, starting from the analytical expression for the transmission coefficient of the SFS equivalent circuit and imposing prescribed design criteria, non-linear systems of equations are formed and solved either numerically or graphically. The obtained geometric parameters are directly employed for our simulations. Lastly, through the systematic deviation between theoretical and numerical outcomes, the design formulas of the previous algorithm [Figure 2(a)], and robust interpolation schemes, we obtain improved expressions for the normalized modal admittances. Again, the accuracy of the final relations can be further increased by repeating the algorithm for a larger number of initial design parameter values, thus escalating the convergence of the interpolation functions.

It should be stressed that our technique is quite general and can also be applied to more complicated arrangements, as for example the multiple fishnet structure (MFS) [27]. In this case, multiple resonances appear due to the interaction of neighboring SFSs, providing a desired behavior for the construction of multiband frequency selective filters.

4. DEVELOPMENT OF THE DESIGN METHODOLOGY

In this section, we extract simple design formulas for the realization of narrowband filters by exploiting the ET phenomenon through an SFS. To this end, according to (1)–(5), parameters x_1 and x_2 must be uniquely determined for any given f_0 and BW (or, equivalently, $Q = f_0/BW$). For these design criteria we impose the limitations $f_0 \in [1, 100]\,\mathrm{GHz}$ and $Q > 100$, since our principal objective is the design of extremely narrowband microwave devices. In what follows, $\log Q$ is used instead of Q, so as to cover the largest possible dynamic range of the quality factor. Also, since the ET phenomenon occurs for frequencies very close to the first Wood-Rayleigh anomaly, we employ

the normalized parameter $\log(1 - x_2) = \log(1 - a/\lambda_0)$ instead of x_2 to better distinguish between the different values as $x_2 \rightarrow 1$. Such choices will be proven particularly instructive in Section 5, where our improvements to the theoretical formulas of (1)–(5) are introduced. Subsequently, our interest focuses on the development of consistent design formulas for the two more typical choices of hole shapes, namely the square (Subsection 4.1) and circular (Subsection 4.2) holes.

The first step of our derivation consists of taking into account numerical simulation results obtained via the Ansys HFSS$^{\text{TM}}$ commercial computational package. The simulation model of the SFS, shown in Figure 3 for square holes, consists of a single unit-cell, where PBCs are applied along the $x = \pm a/2$ and $y = \pm a/2$ planes, to account for the infinite periodicity of the structure. The excitation of a normally incident plane wave for the calculation of the transmission through the structure is provided by two wave ports, placed opposite to it along the z-direction. The reference planes of the respective ports were considered to coincide with the two faces of the SFS. In all the simulations, the entire computational domain has been discretized in around 10.000 tetrahedra on average, as a result of an appropriate adaptive meshing procedure.

4.1. Square Holes

For this specific case, we first conduct simulations for different $x_1 = a/b$ ratios, assuming a constant unit-cell size of $a = 30\,\text{mm}$ while varying the hole size b. The results of this study are summarized
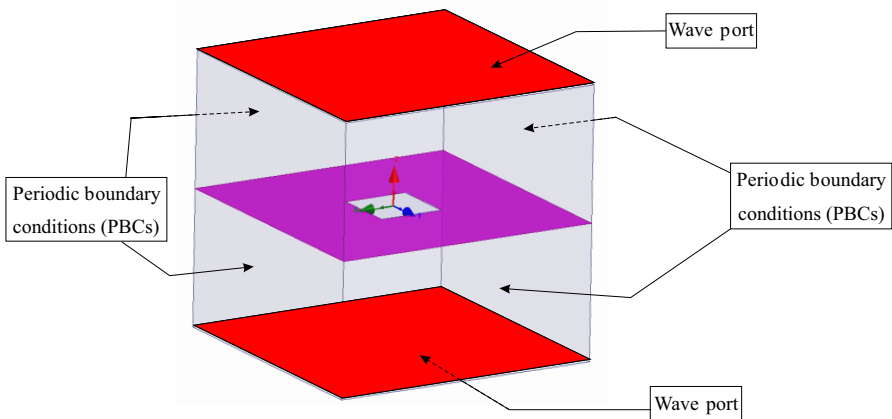

Figure 3. Simulation model for the SFS of Figure 1(b).

in Table 1. Obviously, as x_1 increases, $\log Q$ increases too, while the wavelength at the frequency of the transmission peak, λ_0, approaches a, i.e., $x_2 = a/\lambda_0 \rightarrow 1$. This is in agreement with several recognized reference studies on SFSs [18, 30], according to which as x_1 rises, the transmission peak tends toward the frequency of the first Wood-Rayleigh anomaly ($f_{WR} = c/a$), whereas the bandwidth of the transmission curve becomes narrower. Note that this behavior can be qualitatively predicted from the LC circuit, since for very small holes the corresponding inductance, L, is also small, the capacitance, C, takes large values and the bandwidth of such resonators is known to be very narrow [25]. In other words, due to the fast variation of C over frequency, a small shift of the frequency around the resonance moves the circuit away from its resonance condition.

Table 1. Simulated $\log Q$ and $\log(1 - x_2)$ for various x_1 values, with $a = 30\,\text{mm}$.

x_1	$\log Q$	$\log(1 - x_2)$
3.4	2.4	-1.66
3.8	2.7	-1.82
4.3	3.1	-2.00
4.8	3.5	-2.15
5.3	3.9	-2.28
6.0	4.3	-2.45
6.8	4.7	-2.67
7.5	5.0	-2.78

After these observations, the quantitative analysis of the data provided in Table 1 via curve fitting algorithms, leads to the function that associates x_1 with Q, namely,

$$x_1 = 1.687e^{0.2971 \log Q} \Rightarrow x_1 = 1.687Q^{0.129}, \tag{7}$$

whose root mean square error (RMSE) is 4.8%. On the contrary, the relation between x_2 and Q is given by

$$\log(1 - x_2) = -0.432 \log Q - 0.662 \Rightarrow x_2 = 1 - 0.218Q^{-0.432}, \tag{8}$$

with RMSE = 0.0783%. It becomes apparent that (7) and (8) are the desired design formulas, since the geometric dimensions $a = x_2\lambda_0 = x_2c/f_0$ and $b = a/x_1$ of the SFS can be directly obtained from them in terms of the design criteria (f_0 and Q)[†].

[†] Note that, while the normalized variables x_1 and x_2 can be promptly extracted from Q through (7) and (8), the exact geometric dimensions a and b can be specified only for a given value of f_0, thus further justifying the use of normalized variables.

To verify the preceding formulas, several practical cases are carefully explored. To this end, the proper geometric dimensions, corresponding to a prescribed $f_0 = 30$ GHz center frequency and various $\log Q$ design values, are calculated through these expressions. Then, f_0 and $\log Q$ are, also, retrieved from numerical simulations by means of the already computed a and b values, in order to compare them with the initial design specifications. The results of this technique for six different $\log Q$ values, summarized in Table 2, reveal an almost excellent agreement between the desired and simulated parameters.

Table 2. Relative error of the simulated $\log Q$ and f_0 for the design frequency of $f_0 = 30$ GHz and a, b values derived from (7) and (8).

Design $\log Q$	a (mm)	b (mm)	Simul. $\log Q$	Relative error (%)	Simul. f_0 (GHz)	Relative error (%)
2	9.702	3.175	1.87	6.50	30.03	0.08
3	9.890	2.405	2.81	6.33	29.90	0.33
4	9.959	1.800	4.12	3.00	30.01	0.03
5	9.985	1.340	5.00	0.00	29.99	0.03
6	9.994	1.000	6.15	2.50	29.99	0.04
7	9.998	0.741	7.15	2.14	29.99	0.04

Having satisfactorily validated the accuracy and efficiency of (7) and (8), our analysis concentrates on the linearity of the examined fishnet structure. In fact, the certification of this property is a key issue in the design of high-end filters, since nonlinearities can seriously distort the transmitted signal. For this purpose, the simulated amplitude and phase of the SFS transmission coefficient for $f_0 = 30$ GHz and $\log Q = \{3, 4, 5, 6\}$, with a and b obtained via (7) and (8), are depicted in Figures 4(a)–4(d). Since we are mostly interested in the frequency region associated to the half power bandwidth of the transmission through the SFS, adequate linearity criteria should be provided. To quantify possible deviations from linearity, the arithmetic mean and standard deviation of the simulated transmission phase data from a perfectly linear function are extracted through the application of a linear regression to it. Results are shown in Table 3 for every case in Figures 4(a)–4(d). Evidently, both the arithmetic mean and standard deviation remain very small and, hence, the SFS structure exhibits an almost linear behavior in the region under investigation.
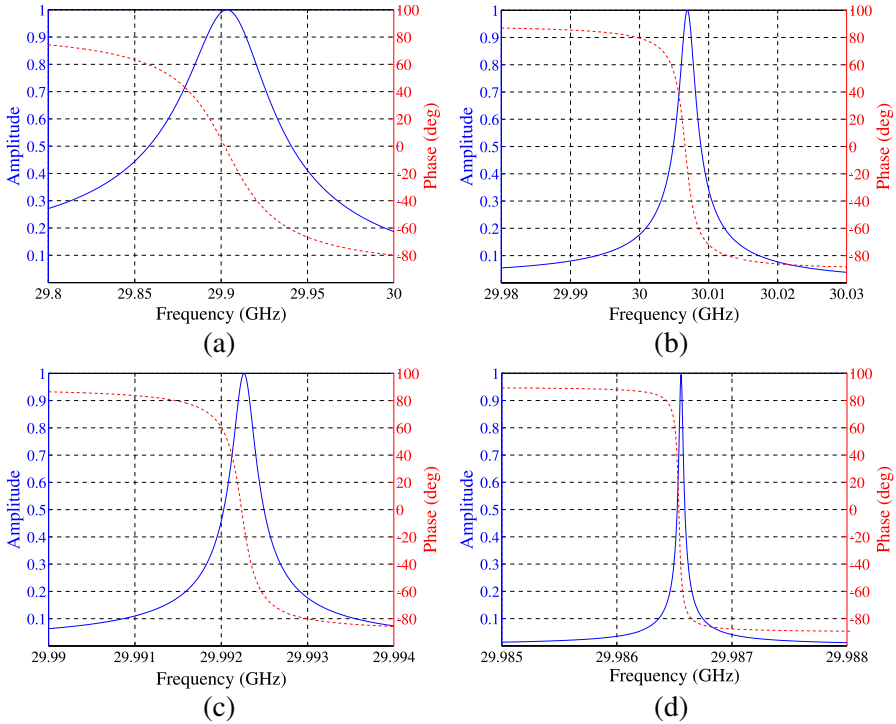
Figure 4. Simulated amplitude (blue solid line) and phase (red dashed line) of the transmission coefficient with $f_0 = 30\,\text{GHz}$ and (a) $\log Q = 3$, (b) $\log Q = 4$, (c) $\log Q = 5$, and (d) $\log Q = 6$, for a, b values obtained from (7) and (8).

Table 3. Arithmetic mean and standard deviation for the discrepancy between the simulated transmission phase of Figures 4(a)–4(d) and the ideal linear phase function.

$\log Q$	Arithmetic mean	Standard deviation
3	$3.42 \cdot 10^{-6}$	1.703
4	0.018	1.844
5	$1.38 \cdot 10^{-5}$	1.838
6	0.037	1.876

Table 4. Simulated $\log Q$ and $\log(1 - x_2)$ for various x_1 values, with $a = 30$ mm.

x_1	$\log Q$	$\log(1 - x_2)$
7	3.08	-1.90
8	3.29	-2.06
9	3.64	-2.22
10	3.96	-2.35
11	4.22	-2.46
12	4.52	-2.58
13	4.70	-2.65
14	5.00	-2.71

4.2. Circular Holes

Proceeding to circular holes, a similar approach can be followed, with the only difference that parameter x_1 is, now, defined as $x_1 = a/r$, where r is the radius of the hole. Hence, in the SFS simulation model of Figure 3, square holes are substituted with circular ones, while the rest of the configuration remains the same. Several numerical simulations are conducted by keeping the unit cell size $a = 30$ mm constant and varying r. The outcomes of this process, given in Table 4, reveal a behavior identical to the case of square holes. Again, by applying curve fitting strategies, we obtain the respective design formulas

$$x_1 = 0.2415 \left(\log Q\right)^2 + 1.627 \log Q - 0.1501, \tag{9}$$

whose root mean square error (RMSE) is 4.8%, and

$$\log\left(1 - x_2\right) = -0.4196 \log Q - 0.6688 \Rightarrow x_2 = 1 - 0.214 Q^{-0.4196}, \tag{10}$$

with RMSE 3.3%. These expressions are also verified for an assortment of design examples, corresponding to a prescribed $f_0 = 30$ GHz center frequency and various $\log Q$ values, as indicated in Table 5. Likewise, a very good agreement between simulation results and design criteria can be promptly detected, especially for smaller hole dimensions. Moreover, the amplitude and phase of the transmission coefficient for the first four cases of Table 5 are presented in Figures 5(a)–5(d). Finally, the linear performance of these filters may be quantitatively certified as in the previous section (not shown here).

After carefully comparing the results for the square and circular holes, it is deduced that the behaviour of the corresponding filters is very similar. In fact, this observation suggests that the shape of the hole does not significantly affect the underlying physics of the ET

Table 5. Relative error of the simulated $\log Q$ and f_0 for the design frequency of $f_0 = 30\,\mathrm{GHz}$ and a, r values derived from (9) and (10).

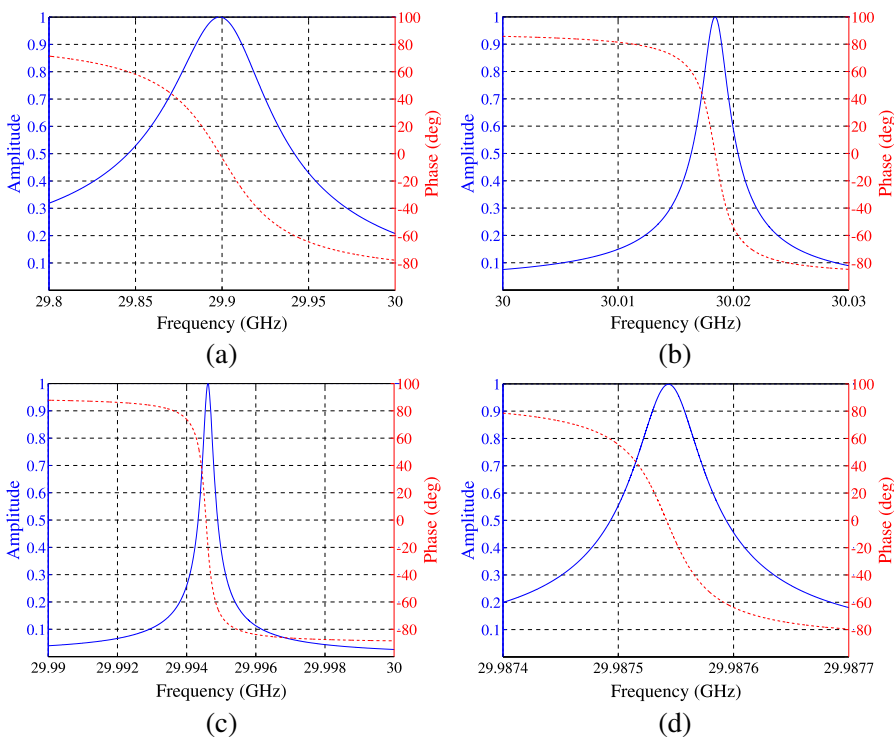| Design $\log Q$	a (mm)	b (mm)	Simul. $\log Q$	Relative error (%)	Simul. f_0 (GHz)	Relative error (%)
3	9.88	1.43	2.72	9.33	29.90	0.33
4	9.96	0.97	4.10	2.50	30.02	0.07
5	9.98	0.71	5.00	0.00	29.99	0.03
6	9.99	0.55	5.79	3.50	29.99	0.03
7	10.0	0.43	6.81	3.17	59.99	0.03

Figure 5. Simulated amplitude (blue solid line) and phase (red dashed line) of the transmission coefficient with $f_0 = 30\,\mathrm{GHz}$ and (a) $\log Q = 3$, (b) $\log Q = 4$, (c) $\log Q = 5$, and (d) $\log Q = 6$, for a, r values obtained from (9) and (10).
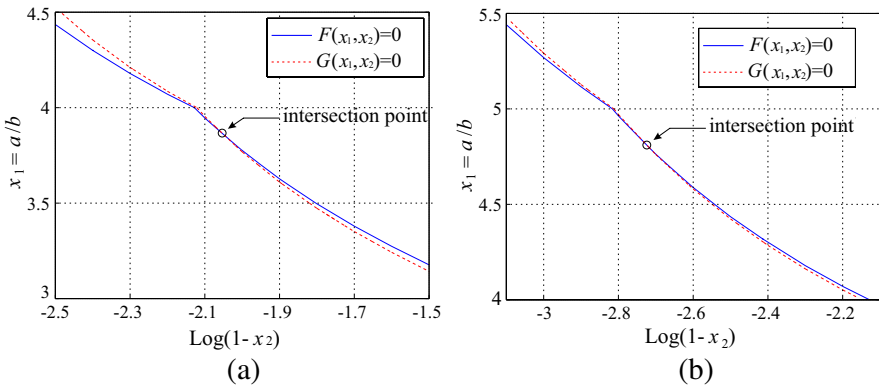
Figure 6. Curves for the $F(x_1, x_2) = 0$ and $G(x_1, x_2) = 0$ contours, defined from (9) and (10), for (a) $\log Q = 3$ and (b) $\log Q = 4$. Their intersection points are approximately located at $(-2.05, 3.8)$ and $(-2.73, 4.8)$, respectively.

phenomenon. The featured approach can also be applied for holes with different geometrical shapes, like an ellipse or a rectangle. However, due to the lack of the four-fold rotational symmetry of the unit cell in those cases, two different polarizations of the incident radiation have to be studied separately [25].

5. ENHANCEMENT OF THE SFS CIRCUIT MODEL EXPRESSIONS

In this section, we take avail of numerical simulations and the previously extracted design formulas to attain appropriate correction factors for the expressions of the equivalent circuit model reported in [26]. Consequently, following from (1)–(5), for any given (f_0, BW) pair, a system of two non-linear analytical equations with two unknown variables, x_1 and x_2, can be formed as

$$T(f_0) = 1 \Rightarrow F(x_1, x_2) = b_C(x_1, x_2) + b_L(x_1, x_2) = 0, \qquad (11)$$

$$T(f_0 + BW/2) = 1/\sqrt{2} \Rightarrow$$

$$G(x_1, x_2) = b_C(x_1, x_2) + b_L(x_1, x_2) - (\sqrt{2} - 1) = 0. \quad (12)$$

The above system may be solved either numerically or, preferably, graphically, i.e., by plotting the non-linear $F(x_1, x_2) = 0$ and $G(x_1, x_2) = 0$ equations and detecting their intersection point[‡]. In this

---

[‡] It should be stated that, since (11) and (12) correspond to specific frequencies f_0 and $f_0 + BW/2$, the normalized admittances, b_C and b_L, depend only on variables x_1 and x_2, as derived from (2) and (3).

Table 6. Theoretical x_1 and $\log(1 - x_2)$ for various $\log Q$ values, as extracted from the graphical solution of (11) and (12).

$\log Q$	x_1	$\log(1 - x_2)$
2.5	3.4	−1.71
3.0	3.8	−2.05
3.5	4.3	−2.40
4.0	4.8	−2.73
4.5	5.3	−3.05
5.0	6.0	−3.30
5.5	6.8	−3.70
6.0	7.5	−4.00

framework, Figures 6(a) and 6(b) depict the solutions for $\log Q = 3$ and $\log Q = 4$, while the results concerning various $\log Q$ are summarized in Table 6. A careful inspection of Tables 6 and Table 1, exhibits a systematic quantitative divergence between their values. Particularly, the transmission peaks acquired from the circuit model of Figure 1(c) are narrower and occur at higher frequencies than their simulated counterparts. This deviation can be accredited to the limited number of high-order modes of (4) and (5), considered from the equivalent circuit model, as an upshot of the small-hole approximation. Therefore, it would be useful to improve the theoretical formulas of Section 2, by employing the outcomes of the previous section, without the need to take into account a larger number of higher-order modes in the approximation of the equivalent circuit. For the sake of clarity, we will refer to the variables of Table 6 with subscript T (theoretical) and to those of Table 1 with subscript S (simulation). Comparing the values of $\log(1 - x_2)$, namely the third column of both tables, and through a linear interpolation scheme, the following formula is obtained

$$\log(1 - x_2)_T = 1.996 \log(1 - x_2)_S + 1.583 \Rightarrow$$
$$(x_2)_T = 1 - 38.28 \left[1 - (x_2)_S\right]^{1.996}, \quad (13)$$

with RMSE = 0.0264%. However, it is readily deduced that (13) in its present form is not practical, since $(x_2)_S$ is not known in advance. To overcome this difficulty, (7) and (8) are combined to yield

$$(x_2)_S = 1 - 1.34 (x_1)^{-3.34}, \quad (14)$$

with a corresponding RMSE = 0.03%. Thus, substituting (14) into (13) and plugging the outcome into (4)–(5), the enhanced relations
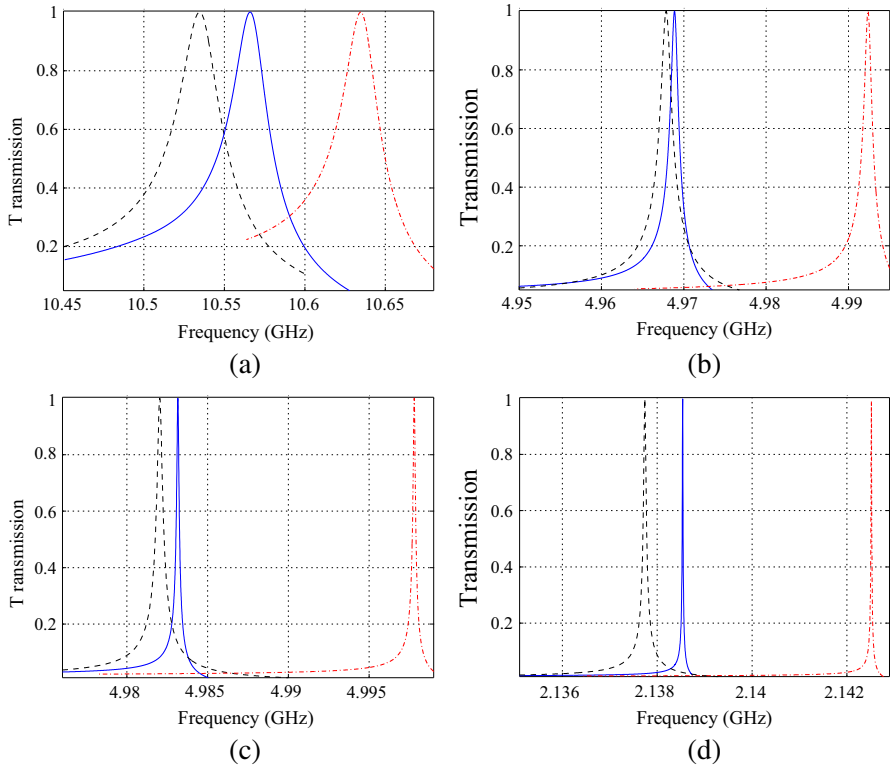
Figure 7. Transmission coefficient for (a) $x_1 = 4$, (b) $x_1 = 5$, (c) $x_1 = 6$, and (d) $x_1 = 7$. Black dashed lines correspond to simulation results, blue solid lines refer to the proposed formulas (15) and (16), while red dash-dotted lines to the relations of [26].

for the normalized modal admittances y^{TM} and y^{TE} are derived

$$y_{n,m}^{\mathrm{TM}} = -j \left\{ \sqrt{\frac{n+m}{(x_3)^2 \left[1 - 68.655 \, (x_1)^{-1.666}\right]^2} - 1} \right\}^{-1}, \quad (15)$$

$$y_{n,m}^{\mathrm{TE}} = j \sqrt{\frac{n+m}{(x_3)^2 \left[1 - 68.655 \, (x_1)^{-1.666}\right]^2} - 1}. \quad (16)$$

To prove the validity of the featured framework, Figures 7(a)–7(d) show the transmission coefficient for $x_1 = \{4, 5, 6, 7\}$, evaluated

via numerical simulations, the relations of [26], and our improved theoretical formulas. As observed, the corrections introduced in (15) and (16) attain a considerable reduction of the frequency shift between the theoretically predicted and the simulated transmission coefficient. Actually, this enhanced approximation can be proven very convenient for the systematic study of SFSs and their profitable application in the design of competent narrowband filters, since it offers an advanced description of the transmission through the structure, without the need of conducting excessive numerical computations. Nevertheless, even these improved formulas are unable to fully capture the exact position of the resonance. This may be attributed to the fact that only a simple linear interpolation scheme based on a few simulation results has been used to extract (13). Such an approximation becomes even better if higher-order polynomials are incorporated instead of this simple linear approximation or by performing additional iterations of the algorithm, as explained in the discussion of Figure 2(b).

6. CONCLUSION

A consistent technique, which successfully exploits the ET phenomenon through single fishnet structures (SFSs) for the effective design of narrowband filters, has been introduced in this paper. The proposed inverse-engineering formulation develops accurate relations that provide the necessary SFS dimensions to achieve a given transmission frequency and half power bandwidth. Thus, the geometric traits of the desired structures are acquired with notably low error levels compared to simulation outcomes. Moreover, by plotting the phase of the transmission coefficient for diverse cases, it has been proven that the SFS does not create significant non-linearities around its operational frequencies. This is a key benefit, since it improves the overall signal integrity of the resulting high-Q filters and circumvents the need for other expensive treatments. On the other hand, to further enhance the efficiency of the existing SFS theoretical circuit model, appropriate correction factors have been derived. In this way, the error in the prediction of the transmission coefficient is considerably reduced, leading to the more robust and reliable characterization of the structure, without increasing the total algorithmic complexity. Finally, it is stressed that the featured methodology can be extended to higher frequencies or even to a broader class of devices, which support the ET phenomenon, given the existence or possible derivation of an equivalent circuit for their theoretical description.

ACKNOWLEDGMENT

REFERENCES

1. Zhang, S., W. Fan, N. C. Panoiu, K. J. Malloy, R. M. Osgood, and S. R. J. Brueck, "Experimental demonstration of near-infrared negative-index metamaterials," *Phys. Rev. Lett.*, Vol. 95, 137404(1–4), 2005.

2. Dolling, G., M. Wegener, C. M. Soukoulis, and S. Linden, "Design-related losses of double-fishnet negative-index photonic metamaterials," *Opt. Express*, Vol. 15, No. 18, 11536–11541, 2007.

3. Navarro-Cía, M., M. Beruete, F. Falcone, M. Sorolla Ayza, and I. Campillo, "Polarization-tunable negative/positive refraction in self-complementariness-based extraordinary transmission prism," *Progress In Electromagnetics Research*, Vol. 103, 101–114, 2010.

4. Cao, T. and M. J. Cryan, "Modeling of optical trapping using double negative index fishnet metamaterials," *Progress In Electromagnetics Research*, Vol. 129, 33–49, 2012.

5. Guo, J., Y. Xiang, X. Dai, and S. Wen, "Enhanced nonlinearities in double-fishnet negative-index photonic metamaterials," *Progress In Electromagnetics Research*, Vol. 136, 269–282, 2013.

6. Mittra, R., C. H. Chan, and T. Cwik, "Techniques for analyzing frequency selective surfaces — A review," *Proc. IEEE*, Vol. 76, No. 12, 1593–1615, 1988.

7. Munk, B. A., *Frequency Selective Surfaces: Theory and Design*, Wiley-Interscience, New York, 2000.

8. Navarro-Cía, M., M. Beruete, F. Falcone, J. Illescas, I. Campillo, and M. Sorolla Ayza, "Mastering the propagation through stacked perforated plates: Subwavelength holes vs. propagating holes," *IEEE Trans. on Antennas and Propag.*, Vol. 59, No. 8, 2980–2988, 2011.

9. Bethe, H. A., "Theory of diffraction by small holes," *Phys. Rev.*, Vol. 66, No. 7–8, 163–182, 1944.

10. Ebbesen, T. W., H. J. Lezec, H. F. Ghaemi, T. Thio, and P. A. Wolff, "Extraordinary optical transmission through sub-wavelength hole arrays," *Nature*, Vol. 391, 667–669, 1998.

11. Song, J. F. and R. Proietti Zaccaria, "Manipulation of light transmission through sub-wavelength hole array," *J. Opt. A: Pure Appl. Opt.*, Vol. 9, No. 9, S450–S457, 2007.

12. Ren, X. F., G. P. Guo, P. Zhang, Y. F. Huang, Z. W. Wang, and G. C. Guo, "Remote control of extraordinary transmission through subwavelength hole arrays," *Europhys. Lett.*, Vol. 84, No. 3, 30005(1–4), 2008.

13. Ghaemi, H. F., T. Thio, D. E. Grupp, T. W. Ebbesen, and H. J. Lezec, "Surface plasmons enhance optical transmission through subwavelength holes," *Phys. Rev. B*, Vol. 58, No. 11, 6779–6782, 1998.

14. Vallius, T., J. Turunen, M. Mansuripur, and S. Honkanen, "Transmission through single subwavelength apertures in thin metal films and effects of surface plasmons," *J. Opt. Soc. Am. A*, Vol. 21, No. 3, 456–463, 2004.

15. Lalanne, P., J. C. Rodier, and J. P. Hugonin, "Surface plasmons of metallic surfaces perforated by nanohole arrays," *J. Opt. A: Pure Appl. Opt.*, Vol. 7, No. 8, 422–426, 2005.

16. Kong, F., K. Li, B.-I. Wu, H. Huang, H. Chen, and J. A. Kong, "Propagation properties of the SPP modes in nanoscale narrow metallic gap, channel, and hole geometries," *Progress In Electromagnetics Research*, Vol. 76, 449–466, 2007.

17. Beruete, M., M. Sorolla, I. Campillo, J. S. Dolado, L. Martín-Moreno, J. Bravo-Abad, and F. J. García-Vidal, "Enhanced millimeter-wave transmission through subwavelength hole arrays," *Opt. Lett.*, Vol. 29, No. 21, 2500–2502, 2004.

18. Martín-Moreno, L., F. J. García-Vidal, H. J. Lezec, K. M. Pellerin, T. Thio, J. B. Pendry, and T. W. Ebbesen, "Theory of extraordinary optical transmission through subwavelength hole arrays," *Phys. Rev. Lett.*, Vol. 86, No. 6, 1114–1117, 2001.

19. García de Abajo, F. J., R. Gómez-Medina, and J. J. Sáenz, "Full transmission through perfect-conductor subwavelength hole arrays," *Phys. Rev. E*, Vol. 72, No. 1, 016608(1–4), 2005.

20. Hongo, K. and Q. A. Naqvi, "Diffraction of electromagnetic wave by disk and circular hole in a perfectly conducting plane," *Progress In Electromagnetics Research*, Vol. 68, 113–150, 2007.

21. Rudnitsky, A. S. and V. M. Serdyuk, "Diffraction of a plane electromagnetic wave by a slot in a conducting screen of finite

thickness placed in front of a half-infinite dielectric," *Progress In Electromagnetics Research*, Vol. 86, 277–290, 2008.

22. Ghazi, G. and M. Shahabadi, "Modal analysis of extraordinary transmission through an array of subwavelength slits," *Progress In Electromagnetics Research*, Vol. 79, 59–74, 2008.

23. Pendry, J. B., L. Martín-Moreno, and F. J. García-Vidal, "Mimicking surface plasmons with structured surfaces," *Science*, Vol. 305, No. 5685, 847–848, 2004.

24. Quevedo-Teruel, O., "Controlled radiation from dielectric slabs over spoof surface plasmon waveguides," *Progress In Electromagnetics Research*, Vol. 140, 169–179, 2013.

25. Medina, F., F. Mesa, and R. Marqués, "Extraordinary transmission through arrays of electrically small holes from a circuit theory perspective," *IEEE Trans. Microw. Theory Tech.*, Vol. 56, No. 12, 3108–3120, 2008.

26. Marqués, R, F. Mesa, L. Jelinek, and F. Medina, "Analytical theory of extraordinary transmission through metallic diffraction screens perforated by small holes," *Opt. Express*, Vol. 17, No. 7, 5571–5579, 2009.

27. Marqués, R., L. Jelinek, F. Mesa, and F. Medina, "Analytical theory of wave propagation through stacked fishnet metamaterials," *Opt. Express*, Vol. 17, No. 14, 11582–11593, 2009.

28. Beruete, M., M. Navarro-Cía, and M. Sorolla Ayza, "Understanding anomalous extraordinary transmission from equivalent circuit and grounded slab concepts," *IEEE Trans. on Microw. Theory and Tech.*, Vol. 59, No. 9, 2180–2188, 2011.

29. Medina, F., J. A. Ruiz-Cruz, F. Mesa, J. M. Rebollar, J. R. Montejo-Garai, and R. Marqués, "Experimental verification of extraordinary transmission without surface plasmons," *Appl. Phys. Lett.*, Vol. 95, No. 7, 071102(1–3), 2009.

30. García de Abajo, F. J., "Colloquium: Light scattering by particle and hole arrays," *Rev. Mod. Phys.*, Vol. 79, No. 4, 1267–1290, 2007.

31. Engheta, N., A. Salandrino, and A. Alù, "Circuit elements at optical frequencies: Nanoinductors, nanocapacitors, and nanoresistors," *Phys. Rev. Lett.*, Vol. 95, No. 9, 095504(1–4), 2005.

32. Huang, C. P., X. G. Yin, H. Huang, and Y. Y. Zhu, "Study of plasmon resonance in a gold nanorod with an LC circuit model," *Opt. Express*, Vol. 17, No. 8, 6407–6413, 2009.